iScience

CellPress

Article

In_2O_3 Nanocrystals for CO_2 Fixation: Atomic-Level Insight into the Role of Grain Boundaries

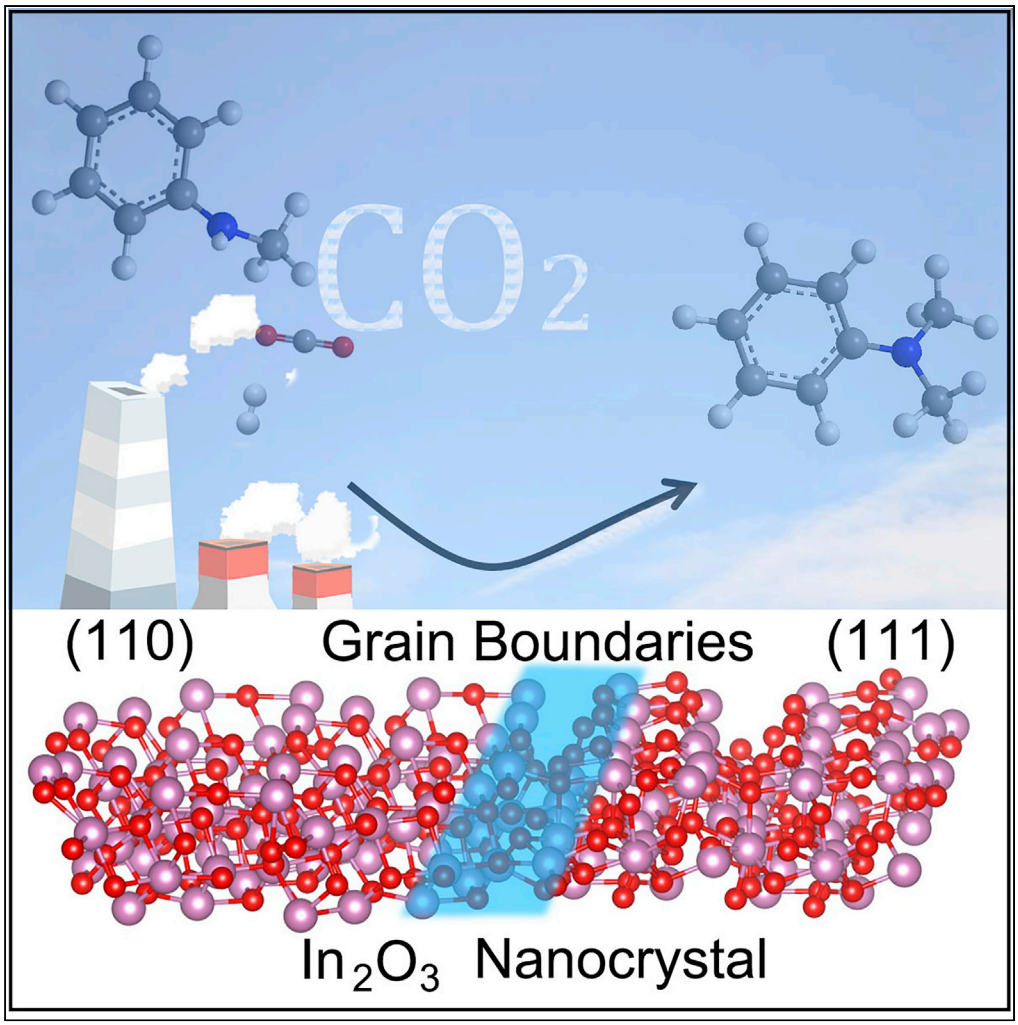

Lirong Wang, Jinyan Cai, Yangcenzi Xie, ..., Leijie Zhang, Shuquan Liang, Liangbing Wang

zxs@ustc.edu.cn (X.Z.)
lsq@csu.edu.cn (S.L.)
wanglb@csu.edu.cn (L.W.)

HIGHLIGHTS

We prepared In_2O_3 nanocrystals with high density of grain boundaries (HGB-In_2O_3)

HGB-In_2O_3 gained 82% yield of N,N-dimethylaniline in N-methylaniline methylation

The grain boundaries in In_2O_3 facilitated the adsorption and activation of CO_2

The grain boundaries in In_2O_3 enhanced the activation of N-H bond in amines

Wang et al., iScience 16, 390–398
June 28, 2019
https://doi.org/10.1016/j.isci.2019.06.005

iScience

CellPress

Article

In_2O_3 Nanocrystals for CO_2 Fixation: Atomic-Level Insight into the Role of Grain Boundaries

Lirong Wang,[1,3] Jinyan Cai,[2,3] Yangcenzi Xie,[1] Jiasheng Guo,[1] Lingxiao Xu,[1] Shuyi Yu,[1] Xusheng Zheng,[2,*] Jian Ye,[2] Junfa Zhu,[2] Leijie Zhang,[2] Shuquan Liang,[1,*] and Liangbing Wang[1,4,*]

SUMMARY

N-functionalization of amines with CO_2 and H_2 is one of the most important processes to make use of CO_2. Although noble metal-based catalysts with remarkable performance have been widely used in this process, developing efficient non-noble-metal-based catalysts remains a grand challenge. Herein, we report In_2O_3 nanocrystals with high density of grain boundaries (HGB-In_2O_3), which show excellent activity toward methylation of amines. Impressively, HGB-In_2O_3 achieved the optimal yield of 82.7% for N,N-dimethylaniline with a mass activity of 21.2 mmol·$g^{-1}h^{-1}$ in methylation of N-methylaniline, comparable to noble-metal-based catalysts. As a bonus, HGB-In_2O_3 held noticeable stability, remarkable selectivity, and comprehensive applicability. Further mechanistic studies revealed that the presence of high density of grain boundaries not only facilitated the adsorption and activation of CO_2 to generate CH_3OH as the intermediate but also enhanced the activation of N-H bond in amines, contributing to the attractive activity of HGB-In_2O_3 toward methylation of amines.

INTRODUCTION

Owing to the superfluous consumption of fossil fuels, anthropogenic emissions of CO_2 to the atmosphere are rapidly increasing, which gives rise to global warming (Bhanja et al., 2018; Molla et al., 2017; Khan et al., 2016; Li et al., 2018). In this case, reduction of CO_2 into fuels utilizing electric (Fernández-Alvarez and Oro, 2018; Goeppert et al., 2014; Liu et al., 2017; Zhang et al., 2019) or solar (Sun et al., 2018; Wang et al., 2018; Hou et al., 2019) energy was considered as an efficient approach to mitigate the environmental problem. Besides, converting CO_2 into high value-added fine chemicals by organic reaction is also an effective way to recycle CO_2, which has attracted intensive attention around the world. In particular, N-functionalization of amines with CO_2 and H_2 is one of the most important processes to make use of CO_2 efficiently (Liu et al., 2015, 2018; Nguyen et al., 2015; Sorribes et al., 2015; Li et al., 2013a, 2013b; Du et al., 2015; Yuan and Lin, 2015; Zhang et al., 2015, 2017; Toyao et al., 2017; Ju et al., 2017; Choi and Hong, 2018; Beydoun et al., 2014; Li et al., 2013a, 2013b; Beydoun et al., 2013; Kon et al., 2014; Cui et al., 2014a, 2014b; Yang et al., 2015; Elangovan et al., 2016; Natte et al., 2017; Cui et al., 2014a, 2014b). Thanks to the efforts from a number of research groups, noble metal-based catalysts including both homogeneous and heterogeneous ones, which have been proved to achieve high activity and selectivity, are mainly used in this process. Typical noble metal-based catalysts for the reaction include Re, Pt, Pd, Ru, Rh, Au, and their complexes (Liu et al., 2015; Nguyen et al., 2015; Sorribes et al., 2015; Li et al., 2013a, 2013b; Du et al., 2015; Yuan and Lin, 2015; Zhang et al., 2015, 2017; Toyao et al., 2017; Ju et al., 2017; Choi and Hong, 2018; Beydoun et al., 2014; Li et al., 2013a, 2013b; Beydoun et al., 2013; Kon et al., 2014; Cui et al., 2014a, 2014b). For instance, a homogeneous well-defined [Ru(triphos)(tmm)] catalyst was reported by Beydoun and coworkers. In the reductive methylation of amines by using CO_2 and H_2, the desired product was isolated with 83% yield (Beydoun et al., 2014). Another notable example is the ruthenium-pincer-type complexes, which were found to attain remarkable turnover numbers of up to 1,940,000 (Zhang et al., 2015). Cui et al. described an efficient procedure for the reductive amination of CO_2 using Pd/$CuZrO_x$ catalyst, which can be realized with up to 97% yield under relatively mild reaction conditions (Cui et al., 2014a, 2014b). As for non-noble-metal-based catalysts, active and high-cost reactants, such as methanol and phenylsilane instead of CO_2 and H_2, were generally required in N-functionalization of amines to achieve the desired catalytic activity (Yang et al., 2015; Elangovan et al., 2016; Natte et al., 2017; Liu et al., 2018; Cui et al., 2014a, 2014b). Therefore developing efficient non-noble-metal-based catalysts for N-functionalization of amines with CO_2 and H_2 remains a grand challenge.

[1]School of Materials Science and Engineering, Key Laboratory of Nonferrous Metal Materials Science and Engineering, Ministry of Education, Central South University, Changsha, Hunan 410083, P. R. China

[2]National Synchrotron Radiation Laboratory, University of Science and Technology of China, Hefei, Anhui 230029, P. R. China

[3]These authors contributed equally

[4]Lead Contact

*Correspondence: zxs@ustc.edu.cn (X.Z.), lsq@csu.edu.cn (S.L.), wanglb@csu.edu.cn (L.W.)

https://doi.org/10.1016/j.isci.2019.06.005

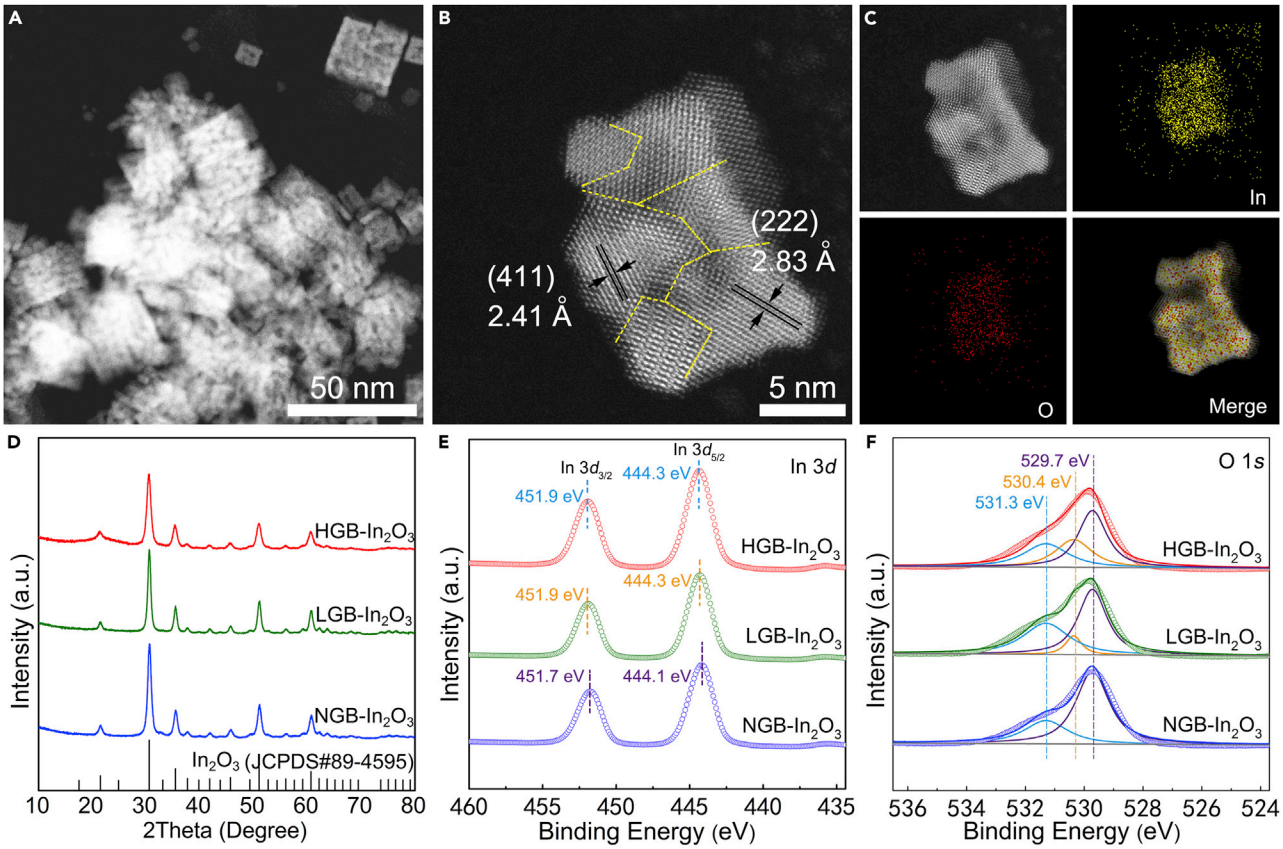

Figure 1. Structural Characterizations of In_2O_3 Nanocrystals

(A) HAADF-STEM image of the HGB-In_2O_3 nanocrystals.

(B) High-resolution HAADF-STEM image of an individual HGB-In_2O_3 nanocrystal.

(C) STEM-energy-dispersive X-ray elemental mapping of an individual HGB-In_2O_3 nanocrystal.

(D) XRD profiles of HGB-In_2O_3, LGB-In_2O_3, and NGB-In_2O_3.

(E) In 3*d* XPS spectra for HGB-In_2O_3, LGB-In_2O_3, and NGB-In_2O_3 nanocrystals.

(F) O 1*s* XPS spectra for HGB-In_2O_3, LGB-In_2O_3, and NGB-In_2O_3 nanocrystals.

Herein, we report a rational design of In_2O_3 nanocrystals with high density of grain boundaries (HGB-In_2O_3), which shows remarkable catalytic performance toward methylation of amines using CO_2 and H_2. During the methylation of N-methylaniline, HGB-In_2O_3 achieved an optimal yield of 82.7% for N,N-dimethylaniline, which is not inferior to noble metal-based catalysts. In addition, 84% of the original reaction activity for HGB-In_2O_3 was preserved after five rounds of reaction. Besides, HGB-In_2O_3 exhibited excellent applicability in the methylation of amines. Further mechanistic studies revealed that the presence of high density of grain boundaries not only facilitated the adsorption and activation of CO_2 to generate CH_3OH as the intermediate, but also enhanced the activation of N-H bond in amines, which led to the attractive catalytic activity of HGB-In_2O_3 toward methylation of amines.

RESULTS

Synthesis and Structural Characterizations of In_2O_3 Nanocrystals

To begin with, the metal-organic frameworks containing indium ions (In-MOFs) were synthesized in a Teflon-lined autoclave at 150°C for 20 h. Figure S1 shows representative scanning electron microscopic (SEM) images of the as-obtained In-MOFs, indicating the formation of stacked structure with single layer having thickness of ~1 μm. In-MOFs were then calcined into powder in a muffle furnace at 350°C and kept for 3 h. Figure 1A shows a high-angle annular dark-field scanning transmission electron microscopic (HAADF-STEM) image of the as-obtained powder. Most of the nanocrystals take a square morphology with an average size of about 14.4 nm (Table S1). The composition and crystalline structure of the as-synthesized

powder were further analyzed by X-ray diffraction (XRD). The XRD profile shown in Figure 1D of the powder can be indexed to a highly crystalline In_2O_3 phase with a body-centered cubic structure (JCPDS#89-4595). Further observation of the high-resolution HAADF-STEM of In_2O_3 displays an individual nanocrystal, in which two sets of fringes with interplanar spacing of 2.41 Å and 2.83 Å are observed, relating to the {411} and {222} planes, respectively. Obviously, the individual nanocrystal is determined to be multiple grains instead of a single grain. As a result, there remains abundant grain boundaries highlighted by yellow dotted lines in Figures 1B and S2. This sample with high density of grain boundaries was named as HGB-In_2O_3. For analysis of the chemical compositions of the nanostructure, the STEM energy-dispersive X-ray elemental mapping images of nanocrystal are shown in Figure 1C, demonstrating the homogeneous distribution of both In and O throughout the nanocrystal. When conducting the synthetic procedure similar to that of the HGB-In_2O_3 except for changing the calcined temperature from 350 to 600°C, nanocrystals with an average size of about 22.2 nm containing grain boundaries were formed (Figure S3 and Table S1). Owing to lower density of grain boundaries compared with HGB-In_2O_3, this sample was named as LGB-In_2O_3. For comparison, In_2O_3 nanocrystals without grain boundaries (NGB-In_2O_3) were also prepared according to a previously reported method (Gao et al., 2017; Albani et al., 2017). These NGB-In_2O_3 nanocrystals have an average size of about 20.2 nm (Figure S4 and Table S1). Besides, the Brunauer-Emmett-Teller surface areas of all samples were also measured (Table S1), where no obvious difference was observed for HGB-In_2O_3, LGB-In_2O_3, and NGB-In_2O_3. In addition, we estimated the density of grain boundary (D_{GB}) of the samples based on the Formulas 1 and 2 in Transparent Methods. Accordingly, the D_{GB} for HGB-In_2O_3 and LGB-In_2O_3 were estimated to be 180,000 and 53,000 m/mg, respectively (Table S1). To characterize the electronic properties of the obtained samples, we conducted X-ray photoelectron spectroscopic (XPS) measurements of In_2O_3. The binding energies of In $3d_{5/2}$ and In $3d_{3/2}$ in HGB-In_2O_3 are 444.3 and 451.9 eV, which are same as that in LGB-In_2O_3 and 0.2 eV higher relative to that in NGB-In_2O_3, respectively (Figure 1E) (Gu et al., 2015; Xu et al., 2007). The O 1*s* XPS spectra of In_2O_3 nanocrystals exhibited three distinct peaks. The prominent peak at 529.7 eV was assigned to O species in internal In_2O_3 nanocrystals. Another binding energy of O 1*s* was 531.3 eV, corresponding to that of the species (such as O_2 and CO_2) adsorbed on the surface of samples. Besides, for HGB-In_2O_3 and LGB-In_2O_3, there existed peak at 530.4 eV, which was assigned to O species in In_2O_3 at grain boundaries (Figure 1F) (Ding et al., 2015).

Catalytic Properties of HGB-In_2O_3 in CO_2 Fixation

The catalytic properties of the as-obtained In_2O_3 were evaluated in methylation of amines using CO_2 and H_2. The model substrate was N-methylaniline leading to N,N-dimethylaniline. Each reaction was performed under 70 bar of mixed gas (CO_2/H_2 = 1:3) at 180°C by using tetrahydrofuran as the solvent. A blank test was conducted without any catalyst, in which no product was observed. Figure 2A illustrates the product yields of adding 25 mg of In_2O_3 catalysts with different density of grain boundaries. When the reaction was catalyzed by HGB-In_2O_3, N,N-dimethylaniline was produced attaining an yield of 82.7% after 9 h. In comparison, the yields decreased to only 21.7% and 12.6% catalyzed by LGB-In_2O_3 and NGB-In_2O_3 under the same reaction condition, respectively. Thus HGB-In_2O_3 catalyst exhibits remarkable activity and selectivity, which was even comparable to the noble metal-based catalysts (Li et al., 2013a, 2013b; Beydoun et al., 2013; Kon et al., 2014; Cui et al., 2014a, 2014b). To further investigate the diversity of catalytic property, we calculated the mass activity for In_2O_3 catalysts at 180°C. As shown in Figure 2B, the mass activity of HGB-In_2O_3 is 21.2 $mmol \cdot g^{-1}\ h^{-1}$, which is almost 4 and 7 times as high as that of LGB-In_2O_3 and NGB-In_2O_3, respectively. We then plotted the profile of the mass activity versus D_{GB} over different catalysts, where an almost linear correlation was observed (Figure S5). This indicated that grain boundaries played the dominated role in catalytic performance. In addition, the stability of HGB-In_2O_3 was also studied by performing successive rounds of reaction. As revealed in Figures 2C and S6, almost 84% of the original reaction activity was preserved after five rounds with product of N,N-dimethylaniline. In addition, the XRD patterns of the recovered HGB-In_2O_3 were also indexed to a highly crystalline In_2O_3 phase (JCPDS#89-4595) (Figure S7A). Although the morphology of the recovered HGB-In_2O_3 had a slight change, grain boundaries in HGB-In_2O_3 were still preserved after five cycles based on the high-resolution HAADF-STEM image (Figure S7B). Both XRD and HAADF-STEM results proved the high stability of HGB-In_2O_3, which is extremely important for potential applications in industrial processes by reducing the cost and pollution efficiently. Furthermore, hot filtration tests showed that the reaction was a heterogeneous catalysis (Figure S8). In the filtrate, only 0.29% of In element relative to HGB-In_2O_3 was leached determined by inductively coupled plasma atomic emission spectrometry. Figure 2D shows a systematic comparison of the methylation of various substituted anilines using HGB-In_2O_3 as catalyst under 70 bar mixed gas (CO_2/H_2 = 1:3) at 180°C for 24 h. When 4-chloroaniline was used as reactant, 4-chloro-N,N-dimethylaniline

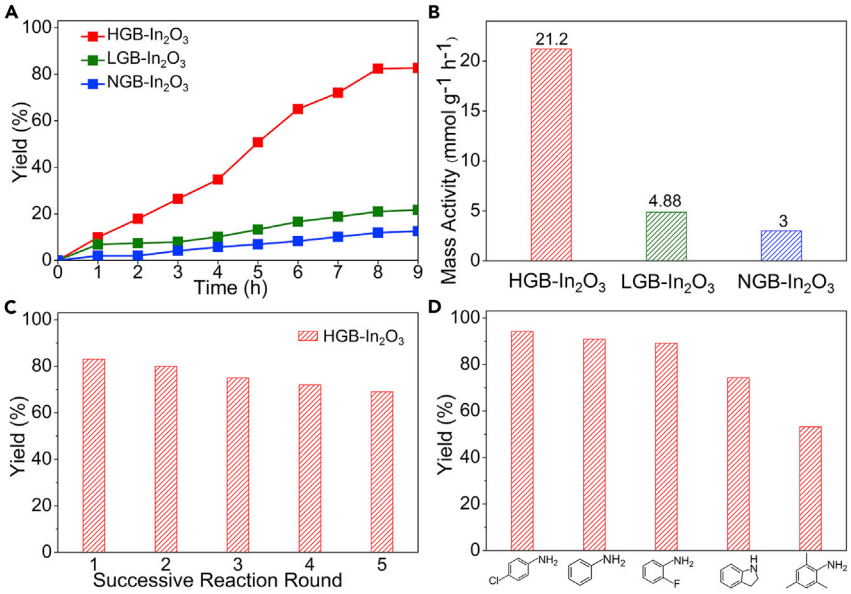

Figure 2. Catalytic Performance of HGB-In_2O_3, LGB-In_2O_3, and NGB-In_2O_3 in CO_2 Fixation

(A) Yield of N,N-dimethylaniline catalyzed by HGB-In_2O_3, LGB-In_2O_3, and NGB-In_2O_3 in methylation of N-methylaniline at 180°C for 9 h.

(B) Comparison of mass activity with HGB-In_2O_3, LGB-In_2O_3, and NGB-In_2O_3 as catalysts in methylation of N-methylaniline at 180°C for 9 h.

(C) Yield of N,N-dimethylaniline catalyzed by HGB-In_2O_3 over the course of five rounds of successive reaction at 180°C for 9 h.

(D) Yields of 4-chloro-N,N-dimethylaniline, N,N-dimethylaniline, N,N-dimethyl-2-fluoroaniline, N-methylindole, and N,N,2,4,6-pentamethylaniline catalyzed by HGB-In_2O_3 in methylation of 4-chloroaniline, aniline, 2-fluoroaniline, indole, and 2,4,6-trimethylaniline at 180°C for 24 h, respectively.

was obtained in high yield of 94.2%. On the contrary, in the transformations of aniline and 2-fluoroaniline, the yields of N,N-dimethylaniline and N,N-dimethyl-2-fluoroaniline slightly dropped to 90.9% and 89.2%, respectively. In addition, 74.3% and 53.2% of indole and 2,4,6-trimethylaniline converted into N-methylindole and N,N,2,4,6-pentamethylaniline, respectively. Notably, when using octylamine as the substrate, 26.3% of conversion was achieved with 99% selectivity of *N*-methyloctan-1-amine. As a result, HGB-In_2O_3 exhibited excellent applicability in the methylation of amines.

Mechanistic Studies of Remarkable Catalytic Activity for HGB-In_2O_3 in CO_2 Fixation

To elucidate the role of grain boundary in catalytic reaction, we investigated the interaction between CO_2 and In_2O_3 catalysts. CO_2 temperature-programmed desorption (CO_2-TPD) measurements of In_2O_3 nanocrystals were implemented. Figure 3A illustrates CO_2-TPD spectra of In_2O_3 catalysts with different densities of grain boundaries. In the presence of HGB-In_2O_3, a prominent peak of desorption appeared at 448°C, which corresponds to the chemisorbed CO_2. For LGB-In_2O_3 and NGB-In_2O_3, two obscure desorption peaks emerging at 455°C and 457°C were in line with chemisorbed CO_2 and the other two weak peaks at around 70°C–80°C conformed to physisorbed CO_2. The adsorption capability was compared on the basis of the peak area lying on the premise of setting the equivalent mass of each sample to 30 mg. The area of chemisorption peak of HGB-In_2O_3 was almost 8 and 11 times larger than that of LGB-In_2O_3 and NGB-In_2O_3, respectively. To further gain insight into the interaction between CO_2 and In_2O_3 catalysts, we carried out *in situ* diffuse reflectance infrared Fourier transform (DRIFT) spectroscopic measurements. After treatment with CO_2 at 180°C for 30 min, the *in situ* DRIFT spectrum of HGB-In_2O_3 exhibited a peak at 1,455 cm^{-1} assigned to CO_3^{2-}* species and another one at 1,285 cm^{-1} assigned to $CO_2^{\delta-}$* (Graciani et al., 2014). With regard to LGB-In_2O_3 and NGB-In_2O_3 after exposure to CO_2 at 180°C for 30 min, peaks at 2,360 cm^{-1} appeared, corresponding to the frequency of physisorbed CO_2* species (Figure 3B) (Wang et al., 2009). As a result, grain boundaries are beneficial to the chemisorption of CO_2. To rationalize the remarkable function of grain boundary in activation of CO_2, we carried out density functional theory (DFT) calculations. One

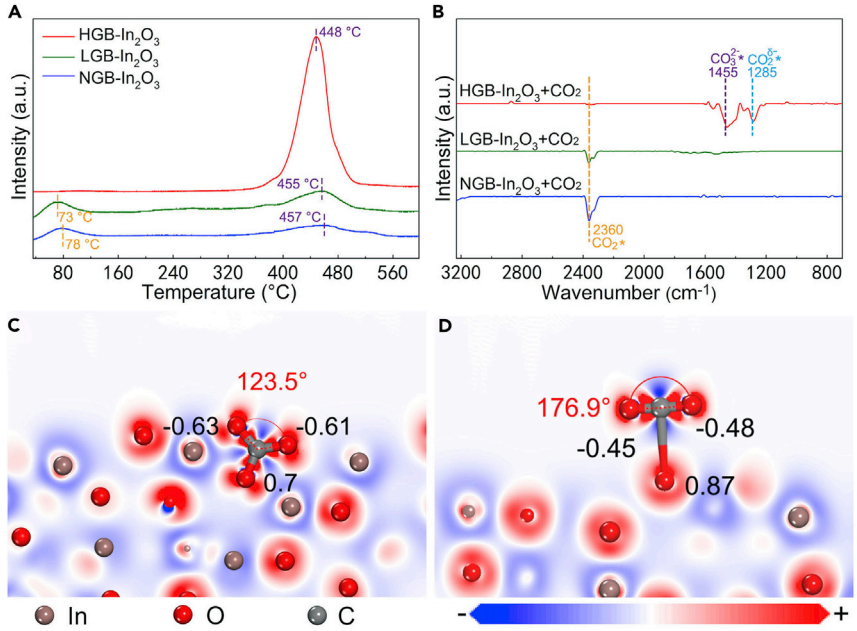

Figure 3. Mechanistic Studies of the Role of Grain Boundary in CO_2 Activation

(A) CO_2-TPD profiles of HGB-In_2O_3, LGB-In_2O_3, and NGB-In_2O_3 nanocrystals.

(B) *In situ* DRIFT spectra of HGB-In_2O_3, LGB-In_2O_3, and NGB-In_2O_3 nanocrystals after treatment with CO_2 at 180°C for 30 min.

(C) The geometrical configurations and electron density difference of CO_2 adsorbed on In_2O_3(GB).

(D) The geometrical configurations and electron density difference of CO_2 adsorbed on In_2O_3(111).

atomic model for single-crystal In_2O_3 was established along the (111) facet, which was named as In_2O_3(111). Another model consisted of two grains formed along (110) and (111) facets, respectively (Figure S9). This model involving a grain boundary was named as In_2O_3(GB). First-principle simulations were performed to calculate the adsorption energies of CO_2 on In_2O_3(111) and In_2O_3(GB). The adsorption energy of CO_2 on In_2O_3(GB) was −1.66 eV, much higher than that on In_2O_3(111) with the value as low as −0.1 eV. Figures 3C and 3D reveal the adsorption geometries of CO_2 on In_2O_3(GB) and In_2O_3(111). For In_2O_3(GB), there exist higher negative charge density of surface O atoms and lower positive charge density of C atoms on the surface than that for In_2O_3(111). Thus, CO_2 obtained more negative electrons when absorbed in In_2O_3(GB), promoting the process of activation. Notably, the interatomic bond angles of CO_2 decreased from 180° to 176.9° and 123.5° on In_2O_3(111) and In_2O_3(GB), respectively. The greater reduction of the bond angle led by grain boundaries increases the internal energy of CO_2 molecule, further making it unstable and prone to reaction. Thus, grain boundaries encourage the adsorption and activation of CO_2. We also performed *in situ* DRIFT measurement to study the activation of H_2. Before recording the DRIFT spectrum, HGB-In_2O_3 was exposed to H_2 (1 bar) at 180°C for 1 h. As shown in DRIFT spectrum, the set of frequencies at 3,660–3,551 cm^{-1} corresponding to the stretching vibration of O-H were observed (Figure S10). It was thus speculated that H_2 was dissociated after adsorbing on the oxygen atoms of In_2O_3.

Furthermore, the interaction between amines and In_2O_3 catalysts was also explored. Figure 4A shows the *in situ* DRIFT spectra of HGB-In_2O_3, LGB-In_2O_3, and NGB-In_2O_3 after treatment with N-methylaniline at 180°C for 30 min. With regard to HGB-In_2O_3, peaks at 692–750, 1,262, 1,506–1,603, 2,904–3,049, and 3,416 cm^{-1} appeared, corresponding to the bending vibration of C-H, the stretching vibrations C-N, the vibration of benzene skeleton, the stretching vibrations of C-H, and the stretching vibration of N-H, respectively. Considering that the fracture of N-H plays a pivotal role in the methylation of amines, we focused on the distinction of peaks for the stretching vibration of N-H among In_2O_3 catalysts. In the spectra of LGB-In_2O_3 and NGB-In_2O_3, the peaks for the stretching vibration of N-H shifted to 3,422 and 3,443 cm^{-1}, respectively. Thus, HGB-In_2O_3 was found to illustrate the lowest wave number of the peaks among the three samples, indicating the largest length of N-H bond. Therefore, grain boundary benefits the activation of N-H bond in amines. DFT calculations were conducted on In_2O_3(GB) and In_2O_3(111) to further verify the function

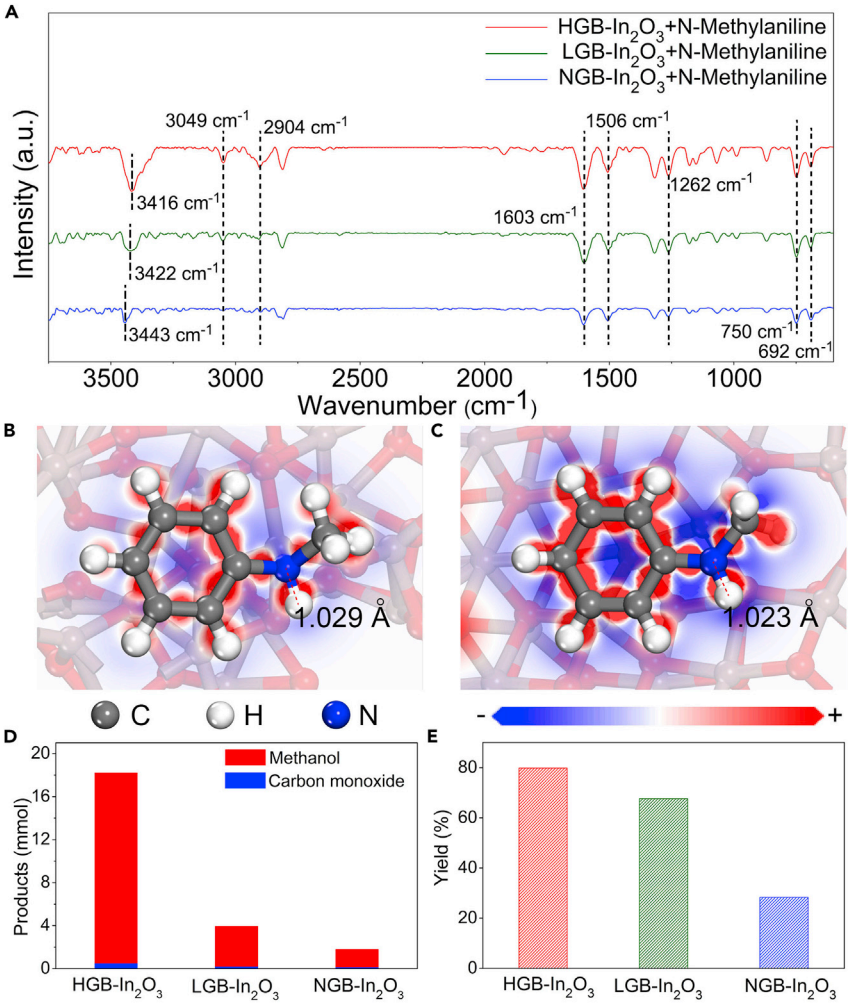

Figure 4. Mechanistic studies of remarkable catalytic activity for HGB-In_2O_3

(A) *In situ* DRIFT spectra of HGB-In_2O_3, LGB-In_2O_3, and NGB-In_2O_3 nanocrystals after treatment with N-methylaniline at 180°C for 30 min.

(B) The geometrical configurations and electron density difference of N-methylaniline adsorbed on In_2O_3(GB).

(C) The geometrical configurations and electron density difference of N-methylaniline adsorbed on In_2O_3(111).

(D) Products of CO_2 hydrogenation over HGB-In_2O_3, LGB-In_2O_3, and NGB-In_2O_3 nanocrystals at 180°C after 8 h.

(E) Yield of N,N-dimethylaniline when CH_3OH and N-methylaniline react at 180°C catalyzed by HGB-In_2O_3, LGB-In_2O_3 and NGB-In_2O_3 for 4 h.

of grain boundary in activating N-H bond. The adsorption energy of N-methylaniline on In_2O_3(GB) was −0.48 eV, implying exothermic adsorption on In_2O_3(GB). In comparison, the adsorption energy of 0.33 eV for In_2O_3(111) demonstrates that the adsorption of N-methylaniline on In_2O_3(111) was endothermic. As shown in Figures 4B and 4C, the length of N-H bond was 1.029 Å when absorbed on In_2O_3(GB), whereas for In_2O_3(111), the length of N-H bond decreased to 1.023 Å. The elongation of bond length was able to induce red-shift of stretching vibration frequency for adsorbed N-methylaniline on In_2O_3(GB), well consistent with the observation in *in situ* DRIFT measurements.

For methylation of amines with CO_2 and H_2, the selectivity for product varies with the intermediate of the reaction. For instance, amide is generated when CO serves as the intermediate, whereas aniline is synthesized by forming CH_3OH intermediate (Li et al., 2013a, 2013b; Cui et al., 2014a, 2014b; Tlili et al., 2014; Dang et al., 2015; Tsarev et al., 2015; Ogata et al., 2018; Fernández-Alvarez et al., 2018; Goeppert et al., 2014; Liu et al., 2017; Zhang et al., 2019). To determine the intermediate for methylation of amines, 70 bars of CO_2/H_2 mixed gas (CO_2:H_2 = 1:3) was allowed to react at 180°C for 8 h with In_2O_3 catalysts. After completion of the

reaction, CH_3OH was detected as the main product except a spot of CO (Figure 4D). Therefore, CH_3OH is considered to be the intermediate, conducive to methylation of amines. In addition, HGB-In_2O_3 was endowed with the highest yield of CH_3OH with a value of 17.7 mmol; owing to this, grain boundary promoted the activation of CO_2 (Figure 4D). *In situ* DRIFT measurement was also employed to further explore the reaction intermediate. After exposing HGB-In_2O_3 to the mixed gas (CO_2:H_2 = 1:3, 1 bar) at 180°C for 1 h, the DRIFT spectrum was recorded. As shown in Figure S10, two sets of frequencies were observed. One set of frequency at 2,360 cm^{-1} corresponded to the physisorbed CO_2* species. The other set of frequencies at 3,645–3,619, 2,968–2,863, 1,580, and 1,050 cm^{-1} corresponded to the stretching vibration of O-H, the stretching vibration of C-H, the bending vibration of C-H, and the stretching vibration of C-O in CH_3OH* species, respectively. This result confirmed that methanol was the intermediate during the catalytic reaction, which was consistent with the previous results (Gao et al., 2017; Ye et al., 2013). Moreover, to rationalize the function of activating amines in the methylation reaction, we applied CH_3OH and N-methylaniline to react at 180°C catalyzed by In_2O_3 catalysts. As shown in Figure 4E, when catalyzed by HGB-In_2O_3, N,N-dimethylaniline was produced attaining the yield of 79.8% after 4 h, 1.2 and 2.8 times higher than those of LGB-In_2O_3 and NGB-In_2O_3, respectively. Thus the activation of amines can indeed control the activity of methylation reaction, which can be facilitated by grain boundaries. Taking the discussion above into account, we proposed the reaction pathway of methylation of amines as illustrated in Figure S11. Collectively, grain boundaries not only facilitated the adsorption and activation of CO_2 to generate CH_3OH as the intermediate (Equation 1, Figure S11) but also enhanced the activation of N-H bond in amines (Equation 3, Figure S11), which led to the attractive catalytic activity of HGB-In_2O_3 toward methylation of amines.

DISCUSSION

In conclusion, given the high cost of noble metal-based catalysts, we reported a rational design of HGB-In_2O_3 nanocrystals, which achieved remarkable catalytic performance toward methylation of amines with CO_2 and H_2. We designed a series of In_2O_3 nanocrystals with different density of grain boundaries, i.e., HGB-In_2O_3, LGB-In_2O_3, and NGB-In_2O_3. During the methylation of N-methylaniline, HGB-In_2O_3 achieved an optimal yield of 82.7% for N,N-dimethylaniline, 3.8 and 6.6 times as high as those of LGB-In_2O_3 and NGB-In_2O_3, respectively. Further mechanistic studies revealed that the presence of high density of grain boundaries not only facilitated the adsorption and activation of CO_2 to generate CH_3OH as the intermediate but also enhanced the activation of N-H bond in amines, which led to the attractive catalytic activity of HGB-In_2O_3 toward methylation of amines. This work not only develops a catalyst with high density of grain boundaries to achieve the methylation of amines but also opens up new possibilities for designing efficient non-noble-metal-based catalysts.

Limitations of the Study

Although HGB-In_2O_3 exhibited excellent catalytic performance in the methylation of aromatic amines, the activity was still unsatisfactory when using fatty amines as substrates.

METHODS

All methods can be found in the accompanying Transparent Methods supplemental file.

SUPPLEMENTAL INFORMATION

Supplemental Information can be found online at https://doi.org/10.1016/j.isci.2019.06.005.

ACKNOWLEDGMENTS

This work was supported by National Natural Science Foundation of China (Grant no. 51801235, 11875258, 11505187), the Start-up Funding of Central South University (No. 502045005), the Fundamental Research Funds for the Central Universities of Central South University (No. 2018zzts402), and the Fundamental Research Funds for the Central Universities (No. WK2310000066, WK2060190081).

AUTHOR CONTRIBUTIONS

Lirong Wang and J.C. equally contributed to this work. Lirong Wang, S.L., and Liangbing Wang designed the studies and wrote the paper. Lirong Wang and L.X. synthesized catalysts. Lirong Wang and S.Y. performed catalytic tests. X.Z., J.G., L.X., and Lirong Wang conducted XRD, TPD, and *in situ* DRIFT

measurements. J.Z., X.Z., J.Y. and L.Z. conducted XPS measurements. J.C. conducted DFT calculations. All authors discussed the results and commented on the manuscript.

DECLARATION OF INTERESTS

The authors declare no competing interests.

Received: February 12, 2019
Revised: May 13, 2019
Accepted: June 3, 2019
Published: June 28, 2019

REFERENCES

Albani, D., Capdevila-Cortada, M., Vile, G., Mitchell, S., Martin, O., Lopez, N., and Perez-Ramirez, J. (2017). Semihydrogenation of acetylene on indium oxide: proposed single-ensemble catalysis. Angew. Chem. Int. Ed. *56*, 10755–10760.

Beydoun, K., vom Stein, T., Klankermayer, J., and Leitner, W. (2013). Ruthenium-catalyzed direct methylation of primary and secondary aromatic amines using carbon dioxide and molecular hydrogen. Angew. Chem. Int. Ed. *52*, 9554–9557.

Beydoun, K., Ghattas, G., Thenert, K., Klankermayer, J., and Leitner, W. (2014). Ruthenium-catalyzed reductive methylation of imines using carbon dioxide and molecular hydrogen. Angew. Chem. Int. Ed. *53*, 11010–11014.

Bhanja, P., Modak, A., and Bhaumik, A. (2018). Supported porous nanomaterials as efficient heterogeneous catalysts for CO_2 fixation reactions. Chemistry *24*, 7278–7297.

Choi, G., and Hong, S.H. (2018). Selective monomethylation of amines with methanol as the C1 source. Angew. Chem. Int. Ed. *57*, 6166–6170.

Cui, X., Zhang, Y., Deng, Y., and Shi, F. (2014a). N-Methylation of amine and nitro compounds with CO_2/H_2 catalyzed by Pd/$CuZrO_x$ under mild reaction conditions. Chem. Commun. (Camb.) *50*, 13521–13524.

Cui, X., Dai, X., Zhang, Y., Deng, Y., and Shi, F. (2014b). Methylation of amines, nitrobenzenes and aromatic nitriles with carbon dioxide and molecular hydrogen. Chem. Sci. *5*, 649–655.

Dang, T.T., Ramalingam, B., and Seayad, A.M. (2015). Efficient ruthenium-catalyzed N-methylation of amines using methanol. ACS Catal. *5*, 4082–4088.

Ding, M., Meng, D., Tang, Y., Liu, C., and Luo, S. (2015). One-dimensional porous Ag/AgBr/TiO_2 nanofibres with enhanced visible light photocatalytic activity. Chem. Pap. *69*, 1411–1420.

Du, X.L., Tang, G., Bao, H.L., Jiang, Z., Zhong, X.H., Su, D.S., and Wang, J.Q. (2015). Direct methylation of amines with carbon dioxide and molecular hydrogen using supported gold catalysts. ChemSusChem *8*, 3489–3496.

Elangovan, S., Neumann, J., Sortais, J.B., Junge, K., Darcel, C., and Beller, M. (2016). Efficient and selective N-alkylation of amines with alcohols catalysed by manganese pincer complexes. Nat. Commun. *7*, 12641–12648.

Fernández-Alvarez, F.J., and Oro, L.A. (2018). Homogeneous catalytic reduction of CO_2 with silicon-hydrides, state of the art. ChemCatChem *10*, 4783–4796.

Gao, P., Li, S., Bu, X., Dang, S., Liu, Z., Wang, H., Zhong, L., Qiu, M., Yang, C., Cai, J., et al. (2017). Direct conversion of CO_2 into liquid fuels with high selectivity over a bifunctional catalyst. Nat. Chem. *9*, 1019–1024.

Goeppert, A., Czaun, M., Jones, J.P., Surya Prakash, G.K., and Olah, G.A. (2014). Recycling of carbon dioxide to methanol and derived products - closing the loop. Chem. Soc. Rev. *43*, 7995–8048.

Graciani, J., Mudiyanselage, K., Xu, F., Baber, A.E., Evans, J., Senanayake, S.D., Stacchiola, D.J., Liu, P., Hrbek, J., Sanz, J.F., and Rodriguze, J.A. (2014). Highly active copper-ceria and copper-ceria-titania catalysts for methanol synthesis from CO_2. Science *345*, 546–550.

Gu, F., Nie, R., Han, D., and Wang, Z. (2015). In_2O_3–graphene nanocomposite based gas sensor for selective detection of NO_2 at room temperature. Sens. Actuator. B Chem. *219*, 94–99.

Hou, T., Luo, N., Cui, Y.-T., Lu, J., Li, L., MacArthur, K.E., Heggen, M., Chen, R., Fan, F., Tian, W., et al. (2019). Selective reduction of CO_2 to CO under visible light by controlling coordination structures of CeO_x-S/$ZnIn_2S_4$ hybrid catalysts. Appl. Catal. B *245*, 262–270.

Ju, P., Chen, J., Chen, A., Chen, L., and Yu, Y. (2017). N-formylation of amines with CO_2 and H_2 using Pd–Au bimetallic catalysts supported on polyaniline-functionalized carbon nanotubes. ACS Sustain. Chem. Eng. *5*, 2516–2528.

Khan, M.U., Wang, L., Liu, Z., Gao, Z., Wang, S., Li, H., Zhang, W., Wang, M., Wang, Z., Ma, C., et al. (2016). Pt_3Co octapods as superior catalysts of CO_2 hydrogenation. Angew. Chem. Int. Ed. *55*, 9548–9552.

Kon, K., Siddiki, S.M., Onodera, W., and Shimizu, K. (2014). Sustainable heterogeneous platinum catalyst for direct methylation of secondary amines by carbon dioxide and hydrogen. Chem. Eur. J. *20*, 6264–6267.

Li, Y., Fang, X., Junge, K., and Beller, M. (2013a). A general catalytic methylation of amines using carbon dioxide. Angew. Chem. Int. Ed. *52*, 9568–9571.

Li, Y., Sorribes, I., Yan, T., Junge, K., and Beller, M. (2013b). Selective methylation of amines with carbon dioxide and H_2. Angew. Chem. Int. Ed. *52*, 12156–12160.

Li, H., Wang, L., Dai, Y., Pu, Z., Lao, Z., Chen, Y., Wang, M., Zheng, X., Zhu, J., Zhang, W., et al. (2018). Synergetic interaction between neighbouring platinum monomers in CO_2 hydrogenation. Nat. Nanotechnol. *13*, 411–417.

Liu, Q., Wu, L., Jackstell, R., and Beller, M. (2015). Using carbon dioxide as a building block in organic synthesis. Nat. Commun. *6*, 5933–5947.

Liu, X.F., Li, X.Y., Qiao, C., Fu, H.C., and He, L.N. (2017). Betaine catalysis for hierarchical reduction of CO_2 with amines and hydrosilane to form formamides, aminals, and methylamines. Angew. Chem. Int. Ed. *56*, 7425–7429.

Liu, W., Sahoo, B., Spannenberg, A., Junge, K., and Beller, M. (2018). Tailored cobalt-catalysts for reductive alkylation of anilines with carboxylic acids under mild conditions. Angew. Chem. Int. Ed. *57*, 11673–11677.

Molla, R.A., Bhanja, P., Ghosh, K., Islam, S.S., Bhaumik, A., and Islam, S.M. (2017). Pd nanoparticles decorated on hypercrosslinked microporous polymer: a highly efficient catalyst for the formylation of amines through carbon dioxide fixation. ChemCatChem *9*, 1939–1946.

Natte, K., Neumann, H., Jagadeesh, R.V., and Beller, M. (2017). Convenient iron-catalyzed reductive aminations without hydrogen for selective synthesis of N-methylamines. Nat. Commun. *8*, 1344–1352.

Nguyen, T.V., Yoo, W.J., and Kobayashi, S. (2015). Effective formylation of amines with carbon dioxide and diphenylsilane catalyzed by chelating bis(tzNHC) rhodium complexes. Angew. Chem. Int. Ed. *54*, 9209–9212.

Ogata, O., Nara, H., Fujiwhara, M., Matsumura, K., and Kayaki, Y. (2018). N-monomethylation of aromatic amines with methanol via PN(H)P-pincer Ru catalysts. Org. Lett. *20*, 3866–3870.

Sorribes, I., Cabrero-Antonino, J.R., Vicent, C., Junge, K., and Beller, M. (2015). Catalytic N-alkylation of amines using carboxylic acids and molecular hydrogen. J. Am. Chem. Soc. *137*, 13580–13587.

Sun, S., Watanabe, M., Wu, J., An, Q., and Ishihara, T. (2018). Ultrathin $WO_3 \cdot 0.33H_2O$ nanotubes for CO_2 photoreduction to acetate with high selectivity. J. Am. Chem. Soc. *140*, 6474–6482.

Tlili, A., Frogneux, X., Blondiaux, E., and Cantat, T. (2014). Creating added value with a waste: methylation of amines with CO_2 and H_2. Angew. Chem. Int. Ed. *53*, 2543–2545.

Toyao, T., Siddiki, S., Morita, Y., Kamachi, T., Touchy, A.S., Onodera, W., Kon, K., Furukawa, S., Ariga, H., Asakura, K., et al. (2017). Rhenium-loaded TiO_2: a highly versatile and chemoselective catalyst for the hydrogenation of carboxylic acid derivatives and the N-methylation of amines using H_2 and CO_2. Chem. Eur. J. *23*, 14848–14859.

Tsarev, V.N., Morioka, Y., Caner, J., Wang, Q., Ushimaru, R., Kudo, A., Naka, H., and Saito, S. (2015). N-methylation of amines with methanol at room temperature. Org. Lett. *17*, 2530–2533.

Wang, X., Schwartz, V., Clark, J.C., Ma, X., Overbury, S.H., Xu, X., and Song, C. (2009). Infrared study of CO_2 sorption over "molecular basket" sorbent consisting of polyethylenimine-modified mesoporous molecular sieve. J. Phys. Chem. C *113*, 7260–7268.

Wang, S., Guan, B.Y., and Lou, X.W.D. (2018). Construction of $ZnIn_2S_4$-In_2O_3 hierarchical tubular heterostructures for efficient CO_2 photoreduction. J. Am. Chem. Soc. *140*, 5037–5040.

Xu, J.Q., Chen, Y.P., Pan, Q.Y., Xiang, Q., Cheng, Z.X., and Dong, X.W. (2007). A new route for preparing corundum-type In_2O_3 nanorods used as gas-sensing materials. Nanotechnology *18*, 115615–115621.

Yang, Z., Yu, B., Zhang, H., Zhao, Y., Ji, G., and Liu, Z. (2015). Fluoro-functionalized polymeric N-heterocyclic carbene-zinc complexes: efficient catalyst for formylation and methylation of amines with CO_2 as a C1-building block. RSC Adv. *5*, 19613–19619.

Ye, J., Liu, C., Mei, D., and Ge, Q. (2013). Active oxygen vacancy site for methanol synthesis from CO_2 hydrogenation on In_2O_3(110): a DFT study. ACS Catal. *3*, 1296–1306.

Yuan, R., and Lin, Z. (2015). Mechanistic insight into the gold-catalyzed carboxylative cyclization of propargylamines. ACS Catal. *5*, 2866–2872.

Zhang, L., Han, Z., Zhao, X., Wang, Z., and Ding, K. (2015). Highly efficient ruthenium-catalyzed N-formylation of amines with H_2 and CO_2. Angew. Chem. Int. Ed. *54*, 6186–6189.

Zhang, Y., Wang, H., Yuan, H., and Shi, F. (2017). Hydroxyl group-regulated active nano-Pd/C catalyst generation via in situ reduction of $Pd(NH_3)_xCl_y$/C for N-formylation of amines with CO_2/H_2. ACS Sustain. Chem. Eng. *5*, 5758–5765.

Zhang, J., Qian, Q., Wang, Y., Asare Bediako, B.B., Cui, M., Yang, G., and Han, B. (2019). Synthesis of acetamides using CO_2, methanol, H_2 and amines. Green. Chem. *21*, 233–237.

ISCI, Volume *16*

Supplemental Information

In_2O_3 Nanocrystals for CO_2 Fixation: Atomic-Level Insight into the Role of Grain Boundaries

Lirong Wang, Jinyan Cai, Yangcenzi Xie, Jiasheng Guo, Lingxiao Xu, Shuyi Yu, Xusheng Zheng, Jian Ye, Junfa Zhu, Leijie Zhang, Shuquan Liang, and Liangbing Wang

Supplemental Figures

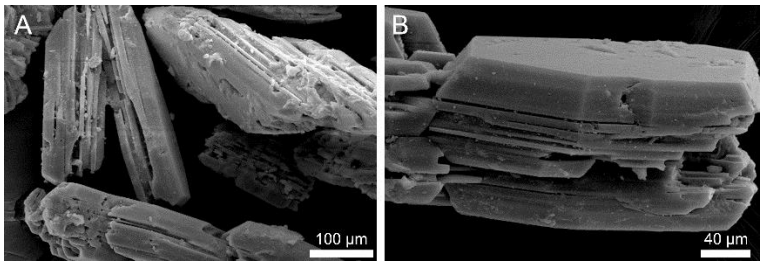

Figure S1. (A, B) SEM images of In-MOFs nanocrystals, related to Figure 1.

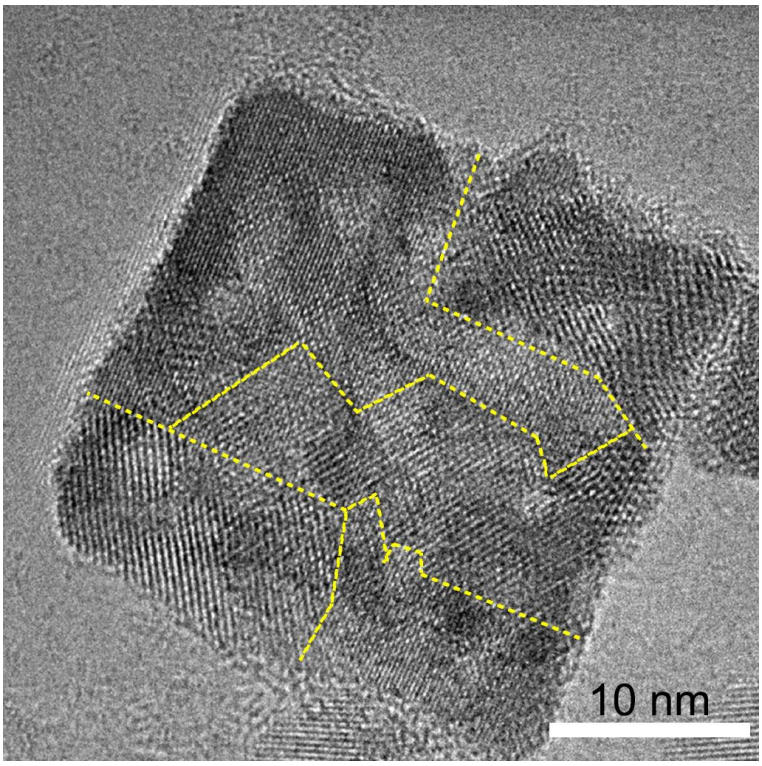

Figure S2. HRTEM image of HGB-In_2O_3, related to Figure 1.

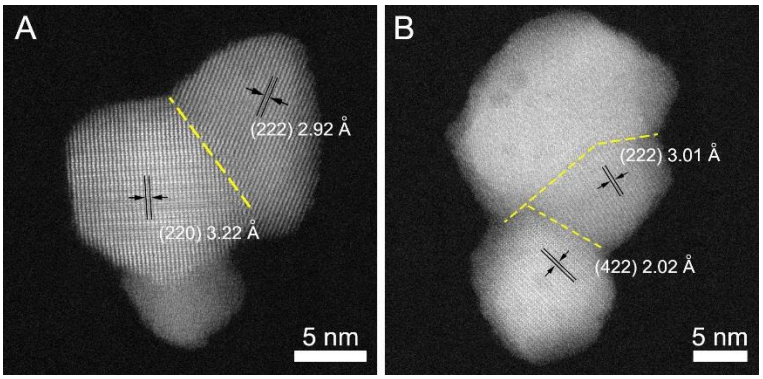

Figure S3. (A, B) High resolution HAADF-STEM images of individual In_2O_3 nanocrystal with low density of grain boundaries, related to Figure 1.

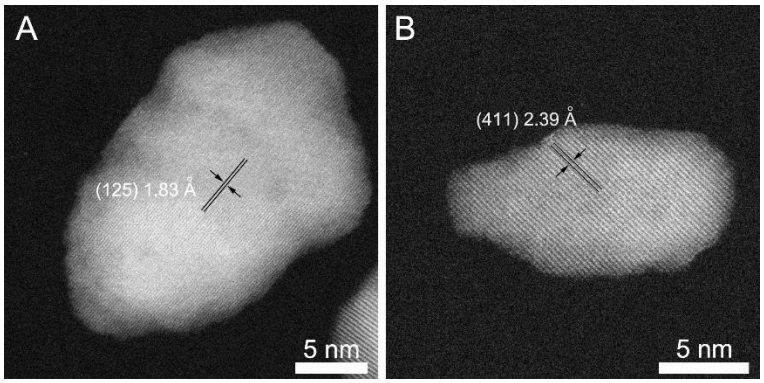

Figure S4. (A, B) High resolution HAADF-STEM images of individual In_2O_3 nanocrystal without grain boundary, related to Figure 1.

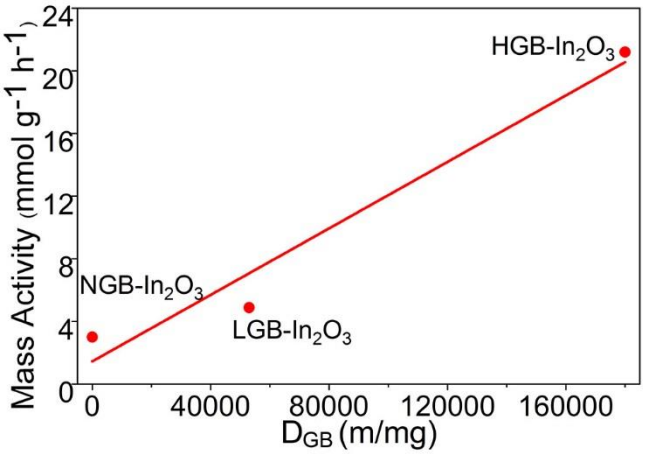

Fugure S5. The plotted profile of the mass activity *versus* D_{GB} over different catalysts, related to Figure 2.

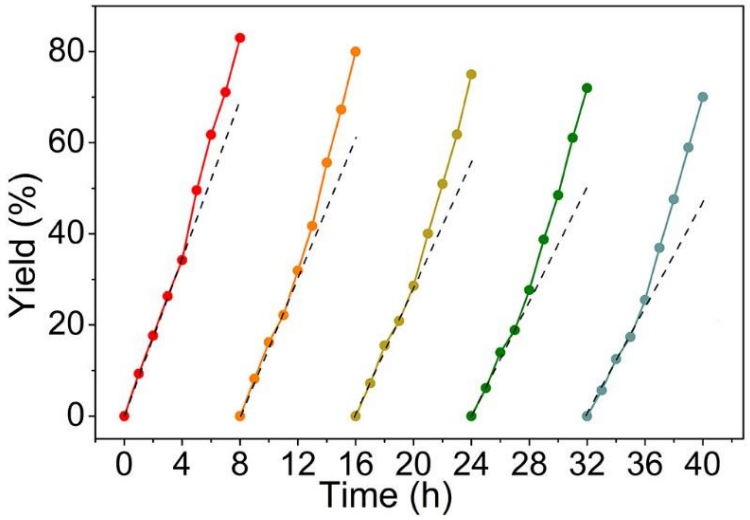

Figure S6. The methylation of N-methylaniline in a 5-cycle repetition, related to Figure 2.

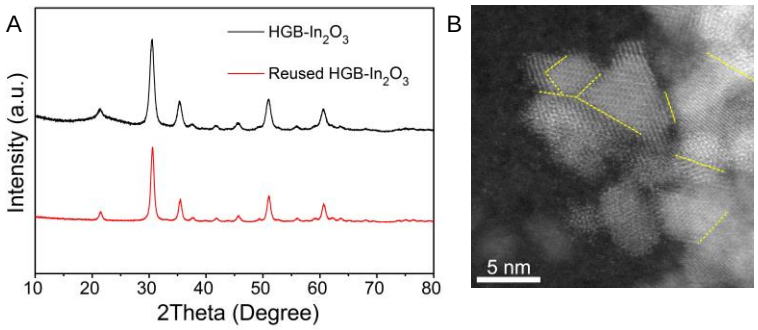

Figure S7. The characterization of the recovered HGB-In_2O_3 by (A) XRD and (B) High resolution HAADF-STEM image, related to Figure 2.

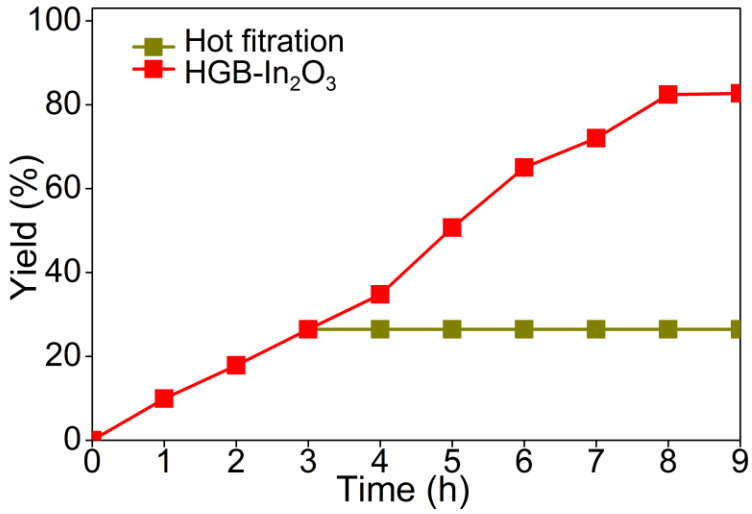

Figure S8. The plotted profile of the yield of product *versus* reaction time and hot filtration experiment over HGB-In_2O_3. In the hot filtration experiment, the reactor was charged and discharged with 70 bar of mixed gas (CO_2/H_2 = 1:3) at room temperature for three times after the addition of 5 mmol of N-methylaniline, 0.5 mmol of bis(trifluoromethylsulfonyl)imide, 25 mg of HGB-In_2O_3 and 40 mL of tetrahydrofuran as solvent. After reacting for 4 h at 180 ºC, the HGB-In_2O_3 was removed by centrifugation at room temperature. The yield of N,N-dimethylaniline was 34.8% analyzed by GC-MS with chlorobenzene as internal standard. The filtrate was then added to the reactor, followed by re-charging 70 bar of mixed gas (CO_2/H_2 = 1:3) at room temperature for three times. As expected, the yield of N,N-dimethylaniline was still maintained to 34.8% after another 4 h. Besides, 0.5 mL of filtrate was used to perform ICP experiment. For HGB-In_2O_3, only 0.29 % of the In element was leached in the filtrate. Based on the above analysis, the methylation of amines over HGB-In_2O_3 was a heterogeneous catalysis, related to Figure 2.

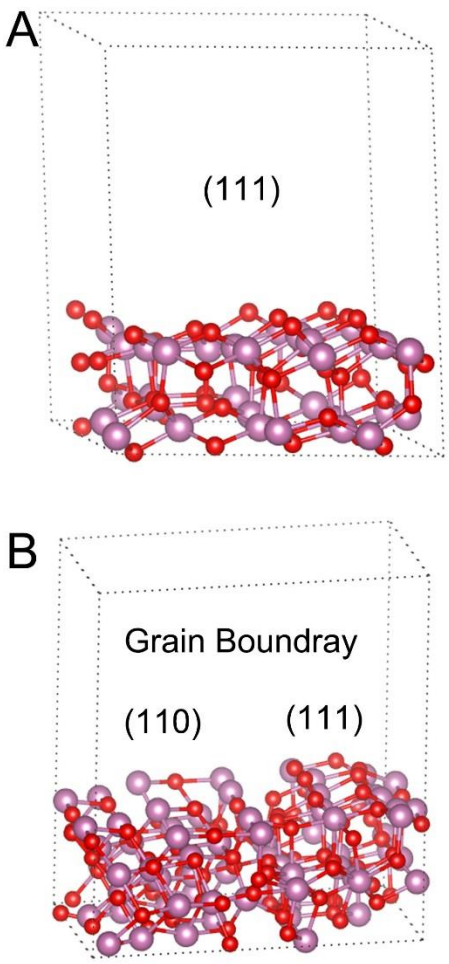

Figure S9. (A) Atomic model for single-crystal In_2O_3 along the (111) facet. (B) Atomic model for two grains formed along (110) and (111) facets, related to Figure 3 and Figure 4.

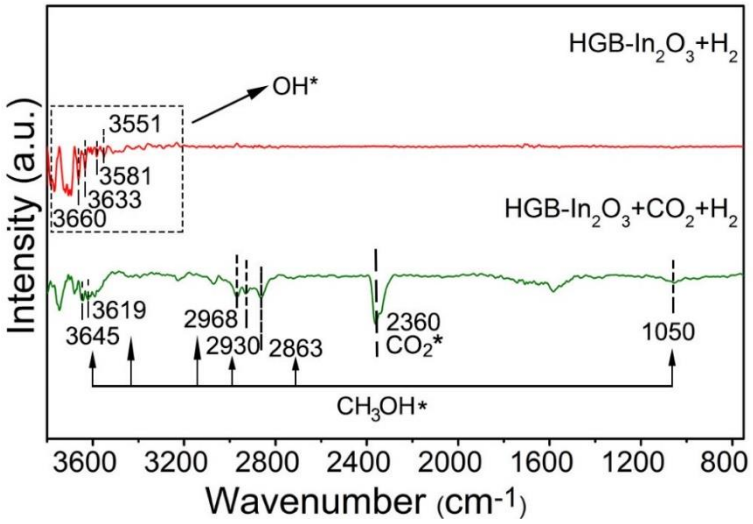

Figure S10. *In situ* DRIFT spectra of HGB-In_2O_3 after the treatment with H_2 (1 bar) and the mixed gas (CO_2:H_2 = 1:3, 1 bar) at 180 °C for 1 h, related to Figure 4.

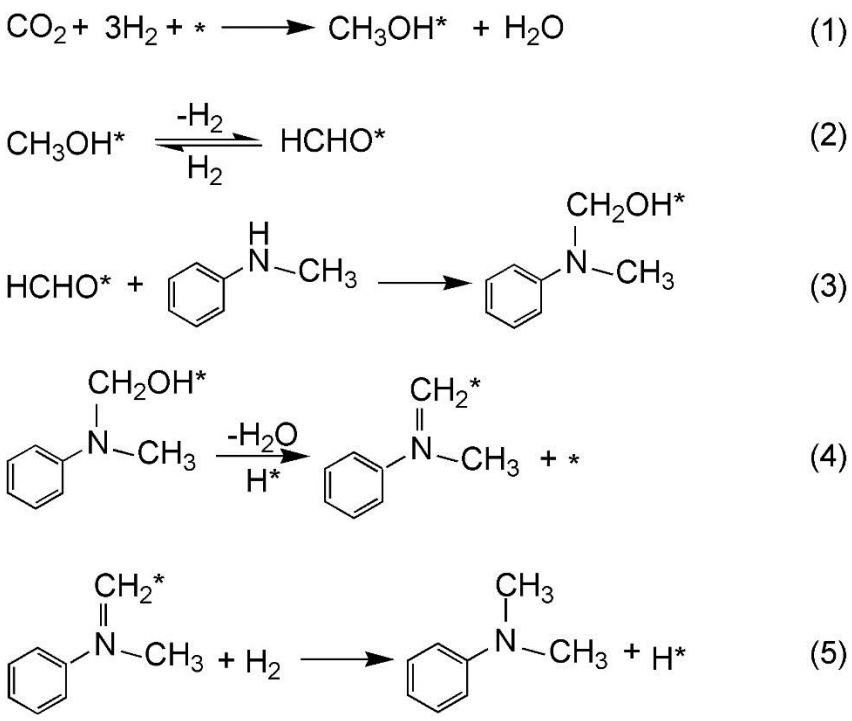

Figure S11. Proposed reaction pathway towards methylation of N-methylaniline with CO_2 and H_2. * represents as an active site, related to Figure 3 and Figure 4.

Table S1. The particle sizes, BET surface areas and D_{GB} of different catalysts, related to Figure 1.

Catalyst	Particle sizes (nm)	BET surface areas (m^2/g)	D_{GB} (m/mg)
HGB-In_2O_3	14.4±2.7	68.13	180,000
LGB-In_2O_3	22.2±4.4	50.61	53,000
NGB-In_2O_3	20.2±3.5	42.61	0

Transparent Methods

Chemicals and materials

Indium(III) acetate ($In(OAc)_3$, 99.9%), 4,4'-bipyridyl (98.0%), 2,2'-biphenyldicarboxylic acid (98.0%), N-methylaniline (98.0%), 4-chloroaniline (≥98.0%), 2,4,6-trimethylaniline (98.0%) and 2-fluoroaniline (99.0%) were obtained from Shanghai Macklin Biochemical Co., Ltd. Indium(III) nitrate 4.5hydrate ($In(NO)_3 \cdot 4.5H_2O$,99.0%), ammonia aqueous (25.0%-28.0%), tetrahydrofuran (99.5%), acetone (≥99.0%), ethanol (≥99.7%), methanol (≥99.5%), indole (99.0%) and aniline (99.5%) were obtained from Shanghai Hushi Laboratorial Equipment Co., Ltd. Bis(trifluoromethylsulfonyl)imide (99.0%) was obtained from Sigma-Aldrich. All chemical reagents were used as received without further purification. All aqueous solutions were prepared using deionized (DI) water with a resistivity of 18.2 $M\Omega \cdot cm^{-1}$.

Preparation of catalysts

HGB-In_2O_3 and LGB-In_2O_3: In-MOFs were synthesized by a previously reported method.[49] Briefly, 3 mmol of indium acetate, 1.62 mmol of 4,4'-bipyridine and 3 mmol of 2,2'-biphenyldicarboxylic acid were dissolved in 45 mL deionized water, followed by stirring for 30 min at room temperature. The solution was transferred into a 50 mL Teflon-lined autoclave, followed by being sealed and heated at 150 ^oC for 20 h. After the mixture was cooled down to room temperature, collecting the precipitate by centrifugation, washing it three times with deionized water, ethanol and acetone respectively and then drying it at 60 ^oC for 12 h. In a typical synthesis of HGB-In_2O_3, the obtained In-MOFs were calcined in muffle furnace at 350 ^oC for 3 h. Further HAADF-STEM image of product determined that there existed high density of grain boundaries. The synthetic procedure of LGB-In_2O_3 was similar to that of HGB-In_2O_3 except for raising the calcined temperature to 600 ^oC.

NGB-In_2O_3: NGB-In_2O_3 was synthesized by a previously reported method (Albani et al., 2017). Briefly, 2 mmol of $In(NO_3)_3 \cdot 4.5H_2O$ was dissolved in a mixture of deionized water (4 mL) and ethanol (12 mL), followed by the addition of the mixture of ammonia (3 mL, 25.0%-28.0%) and ethanol (9 mL) at room temperature. The resulting slurry was stirred for 10 min at 80 ^oC, before collecting the precipitate by filtration and washing it three times with deionized water and ethanol. The obtaining solid was dried at 60 ^oC. Afterwards, the powder was placed into muffle furnace,

followed by calcining at 400 ºC for 3 h.

Estimation of the DGB for different catalysts

The D_{GB} was estimated according to the following formulas:

$$D_{GB} = \frac{L_{GB}}{S_{grain-urface}} * \frac{S_{catalysts}}{M_{catalysts}} \quad (1)$$

$$\frac{S_{catalysts}}{M_{catalysts}} = \frac{\text{total surface area of catalysts}}{\text{total mass of catalysts}} = \text{BET surface area} \quad (2)$$

Where L_{GB} and $S_{grain-urface}$ represent the length of GB and particle area determined by HRTEM and HAADF-STEM images, respectively. $S_{catalysts}$ and $M_{catalysts}$ represent the total surface area and the total mass of the catalysts, respectively.

Catalytic tests

The methylation of amines was performed in a 200 mL automatic constant pressure reactor (Anhui Kemi Machinery Technology Company). In a typical catalytic test, the reactor was charged and discharged with 70 bar of mixed gas (CO_2/H_2 = 1:3) at room temperature for three times after the addition of 5 mmol of N-methylaniline, 0.5 mmol of bis(trifluoromethylsulfonyl)imide, 25 mg of catalysts and 40 mL of tetrahydrofuran as solvent. The reaction proceeded under stirring at 180 ºC for 9 h. After the completion of the reaction, the liquid phase of the reaction mixture was collected by centrifugation at 12,000 r.p.m. for 5 min, and analyzed by GC–MS (QP2010 Ultra, Shimadzu Corporation, Kyoto, Japan) by using chlorobenzene as internal standard. To test the stability of the catalysts, we conducted successive reaction rounds. The catalytic reaction proceeded at 180 ºC for 9 h. After one round, the products were detected, while the catalysts were collected by centrifugation and washed three times with alcohol, followed by re-adding to the reactor for the next round. In addition, 4-chloroaniline, aniline, 2-fluoroaniline, 2,4,6-trimethylaniline and indole participated in the methylation as the reactants in turn under 70 bar of mixed gas (CO_2/H_2 = 1:3) at 180 ºC for 24 h.

The reaction of CO_2 and H_2 was performed in a 200 mL automatic constant pressure reactor (Anhui Kemi Machinery Technology Company). In a typical catalytic test, the reactor was charged and discharged with 70 bar of mixed gas (CO_2/H_2 = 1:3) at room temperature for three times after the addition of 25 mg of catalysts and 40 mL of tetrahydrofuran as solvent. The reaction proceeded

under stirring at 180 °C for 8 h. After the completion of the reaction, the gas phase was determined by gas chromatography (GC-2014C, Shimadzu Corporation, Kyoto, Japan) and a spot of CO were detected. The liquid phase of the reaction mixture was collected by centrifugation at 12,000 r.p.m. for 5 min. 1 mmol of N,N-dimethylformamide was introduced to 1 mL of the reaction mixture as an internal standard. 50 μL of the mixture was dissolved in 0.5 mL of DMSO-d_6 to determine the liquid product by ^{1}H NMR spectroscopy.

With regard to the reaction of N-methylaniline and methanol over In_2O_3 catalysts, 3.6 mmol of methanol and 3 mmol of N-methylaniline were mixed in a 200 mL automatic constant pressure reactor after the addition of 25 mg of catalysts and 40 mL of tetrahydrofuran as solvent, followed by being sealed and heated at 180 °C for 4 h. After the completion of the reaction, the liquid phase of the reaction mixture was collected by centrifugation at 12,000 r.p.m. for 5 min, and analyzed by GC–MS (QP2010 Ultra, Shimadzu Corporation, Kyoto, Japan).

The mass activities shown in Figure 2B were calculated according to the following formula:

$$\text{The mass activity} = \frac{N_{\text{N,N-Dimethylaniline}}}{M_{\text{catalyst}} * h} \quad (3)$$

Where $N_{\text{N,N-Dimethylaniline}}$, M_{catalyst} and h represent the consumed amount of N, N-Dimethylaniline, the mass of the used catalysts and the reaction time (8 h).

In-situ DRIFT tests

In-situ DRIFTS experiments were conducted in an elevated-pressure cell (Harrick DRK-4-BR4) with a Fourier transform infrared spectrometer (Bruker TENSOR II) at 180 °C. After flowing 1 atm of N_2 at the rate of 50 sccm at 180 °C for 0.5 h, the background spectra of the samples were acquired. Then, 1 atm of CO_2 was allowed to flow into cell at 180 °C for 0.5 h. Afterwards, 1 atm of N_2 was allowed to flow into the cell at the rate of 50 sccm for 0.5 h. *In situ* DRIFT spectra of the samples after the treatment with CO_2 were obtained. In addition, for the treatment of the samples with N-methylaniline, the background spectrum of the sample was acquired after flowing with 1 bar of N_2 for 0.5 h at 180 °C. Then the N_2 were allowed to bubble in N-methylaniline solution, followed by flowing into the cell at a rate of 50 sccm at 180 °C for 0.5 h, to bring the saturated N-methylaniline vapor into the cell. Afterwards, 1 atm of N_2 was allowed to flow into the cell at the rate of 50 sccm for 0.5 h. *In situ* DRIFT spectra of the samples after the treatment with N-methylaniline were obtained.

DFT calculations

All density functional theory (DFT) calculations were carried out using CASTEP module as implemented in the Materials Studios package of Accelrys Inc (Clark et al., 2005). Generalized gradient approximation (GGA) with Perdew-Burke-Ernzerhof (PBE) functional was employed for the electron exchange-correlation potential. The ultrasoft pseudopotentials was employed and the core electrons of atoms were treated using effective core potential (ECP). 400 eV kinetic energy cutoff was assigned to the plane-wave basis set. The Brillouin zone was sampled by 2 * 2 * 1 Monkhorst-Pack mesh k-points for surface calculations. The convergence tolerances were set to $5.0 * 10^{-4}$ eV per atom for energy, $5.0 * 10^{-4}$ Å for maximum displacement, and 0.01 eV $Å^{-1}$ for maximum force. The vacuum width is 12 Å between the slabs along the Z axis. All atoms were relaxed during the geometry optimizations. The grain boundary was consisted with (111) and (110) surface. The binding energy of adsorbate (CO_2 or C_7H_9N) on surfaces ($E_{adsorbate*}$) were calculated by $E_{adsorbate*} = E_{adsorbate*+surface} - E_{surface} - E_{adsorbate}$. Here $E_{adsorbate*+surface}$ is the total energy of a surface covered with the adsorbate. $E_{surface}$ is the energy of a surface. $E_{adsorbate}$ is the energy of the adsorbate in the gas phase (Nie et al., 2018).

Instruments

TEM, HAADF-STEM, and STEM-EDX images were collected on a JEOL ARM-200F field-emission transmission electron microscope operating at 200 kV accelerating voltage. X-ray diffraction (XRD) patterns were recorded by using a Philips X'Pert Pro Super diffractometer with Cu-Kα radiation (λ = 1.54178 Å). The BET surface areas of the samples were measured on a Micromeritics ASAP 2460 adsorption apparatus. X-ray photoemission spectroscopy experiments were conducted at the Catalysis and Surface Science Endstation connected to the BL11U beamline in the National Synchrotron Radiation Laboratory (NSRL) in Hefei, China. TPD profiles were recorded by a VDsorb-91i chemisorption analyser.

Supplemental References

Albani, D., Capdevila-Cortada, M., Vile, G., Mitchell, S., Martin, O., Lopez, N. and Perez-Ramirez, J. (2017). Semihydrogenation of Acetylene on Indium Oxide: Proposed Single-Ensemble Catalysis. Angew. Chem. Int. Ed. *56*, 10755-10760.

Clark, S. J., Segall, M. D., Pickard, C. J., Hasnip, P. J., Probert, M. I., Refson, K., and Payne, M. C. (2005). First principles methods using CASTEP. Kristallogr., *220*, 567-570.

Nie, X., Jiang, X., Wang, H., Luo, W., Janik, M. J., Chen, Y., Guo, X. and Song, C. (2018). Mechanistic Understanding of Alloy Effect and Water Promotion for Pd-Cu Bimetallic Catalysts in CO_2 Hydrogenation to Methanol. Acs Catal. *8*, 4873-4892.